International Journal of Heat and Technology
Vol. 44, No. 1, February, 2026, pp. 178-188
Journal homepage: http://iieta.org/journals/ijht

Numerical Investigation of Radial Turbine Flow Characteristics and Efficiency Using ANSYS CFX

Qusai Noori Irmish[1*], Layth H. Jawad[2]

[1] Department of Power Engineering Techniques, AL-Mussaib Technical College, Babil 51006, Iraq
[2] Department of Renewable Energy Engineering Techniques, Polytechnic College Karbala, Karbala 56001, Iraq

Corresponding Author Email: qusay.noori.tcm96@student.atu.edu.iq

https://doi.org/10.18280/ijht.440115

Received: 31 August 2025
Revised: 27 November 2025
Accepted: 10 December 2025
Available online: 28 February 2026

Keywords:
radial turbine, Computational Fluid Dynamics, ANSYS CFX, efficiency, flow characteristics, performance analysis

ABSTRACT

The present investigation was a comprehensive numerical study of a radial turbine conducted using Computational Fluid Dynamics (CFD) in ANSYS CFX. Vista RTD provided the aerodynamic geometry of the turbine, and a structured mesh was created using BladeGen and TurboGrid. Mesh independence was established with about 1.45 million elements, resulting in a variation of power output of less than 0.5 percent. To predict the three-dimensional flow field, the Reynolds-Averaged Navier-Stokes (RANS) equations were solved using the standard k-ε turbulence model. The analysis considered a variety of operating conditions, including three inlet flow angles (50°, 60°, and 70°), expansion ratios ranging from 1.6 to 2.8, and rotational speeds of 30,000 rpm, 60,000 rpm, and 90,000 rpm. The results showed a significant effect of these parameters on the turbine's aerodynamic performance. At a rotational speed of 30,000 rpm, the efficiency was increased from 0.26 to 0.45. At 90,000 revolutions per minute, the ratio of expansion was 2.8; after this, the most excellent was 0.63, or a 142 percent increase. Power output was also increased along with rotational speed, from 710.63 W with a rotational speed of 30000 rpm to 3.29 kW with a rotational speed of 90000 rpm (an increase of 362% with an expansion ratio of 2.8). Flow contours indicated that at higher speeds, the rate of flow velocity and pressure levels were much higher, i.e., 210 m/sec and 130 Pa, respectively. These conditions were accompanied by secondary flows and recirculation, which restricted the overall efficiency. Overall, the results implied a good trade-off between power-generating efficiency and flow stability. They also gave practical suggestions on the application of radial turbines in turbochargers, microturbines, and organic Rankine cycles.

1. INTRODUCTION

The development of the internal combustion engine (ICE) in the latter few decades has been significantly influenced by environmental factors, particularly a reduction in greenhouse gas emissions and decreased fuel consumption. Around the world, regulations have become more burdensome regarding the application of CO_2 emission standards in newly purchased cars, leading producers to invest more in advanced technologies that favor downsizing, which in turn preserves performance [1, 2]. One of the most effective solutions developed is turbocharging, a technique that increases the air flow rate into the engine, resulting in higher power and torque values for a given engine size [3, 4]. In the past, turbochargers were primarily implemented to increase engine performance, but they have now evolved to ensure engine efficiency and meet emission standards [5]. Using lean boosting with turbocharging helps reduce CO_2 emissions while improving fuel efficiency [6]. Among all the turbocharger technologies, the most well-known is the fixed geometry turbocharger (FGT), which has a turbine and a compressor connected via a fixed standard shaft [7]. Although FGTs are a relatively straightforward and proven technology, they are marred by considerable disadvantages, in particular, their low-end torque is very bad, not to mention an intense turbo lag [7, 8]. These deficiencies have led to the development of variable geometry turbochargers (VGTs), which adjust the effective flow area through the turbine or compressor to achieve optimum operation over a wide range of operating conditions. VGTs have been highly successful in reducing turbo lag, increasing low-speed torque, and improving efficiency [9]. Economic comparisons against electrically assisted systems, as well as supercharging, have strengthened the case for VGTs in bold boosting strategies. Galloway et al. [10] performed a numerical optimization of the vane aerodynamics in nozzles by using the software DesignXplorer and ANSYS CFX. Their study showed that secondary losses can be decreased by as much as 12% and the turbine efficiency increased by about 4.5% by optimizing the vane angle, chord, and thickness.

Asanaka et al. [11] examined the effects of nozzle clearance variation on the variable geometry turbines (VGTs). They determined that losses due to hub clearance were approximately 6% and that losses due to shroud leakage vortices were approximately 10% of the efficiency. This brings us to the importance of shroud clearance in terms of efficiency. Danlos et al. [12] experimentally studied the

control of the surge by varying nozzle geometry. Their results showed that VGT mechanisms increased the surge-free operation by almost 15% of the mass flow range and reduced the pressure oscillations by 20% under transient states. Gupta et al. [13] proposed an adjustable geometry nozzle-rotor system, which was experimentally verified using Computational Fluid Dynamics (CFD). Their results showed efficiency improvements of between 2% and 7%, as well as improved alignment of the flow from the turbines, resulting in power output increases of up to 6%. Lee et al. [14], in their investigation of the use of pivoting vanes in a turbocharger in diesel engines, involved the use of modeling as well as testing. His research revealed an improvement in transient response time of nearly 18%, and at low speeds, the torque supply increased by 12%, demonstrating the merits of the pivoting design. Stefanopoulou et al. [15] investigated the cooperation between the control of VGT and the exhaust gas recirculation (EGR) system. Their results showed a reduction of up to 35 percent in NOx emissions (though they came at the cost of a 3 percent reduction in fuel efficiency), pointing to one of the trade-offs between emission reduction and engine performance. Zhao et al. [16] used a variable geometry inlet orifice before the compressor. They showed an improvement of the margin of the surge, 25%, but at higher evaluations of the flow, the maximum efficiency dropped by nearly 2%. Tamaki and Yamaguchi [17] studied the employed variable diffuser vanes in compressors. Their research showed that vane control not only reduced the symmetric surge initiation to 20% of the flow capacity but also increased the range of the stable operation by 15%. In addition, the effect on efficiency was negligible. Ludtke [18] had experimentally verified the usefulness of vaneless diffusers. The results showed that the margin has increased by 18%; however, there was a reduction in overall efficiency of between 5% and 7% compared to traditional vaned designs.

Whitfield et al. [19] made a theoretical study of diffuser configurations. They found that for vaneless diffusers, stability increased by 15%, while pressure recovery rose by almost 8% for vaned diffusers. Abdelhamit [20] conducted a study on throat control in centrifugal diffusers, concluding that dynamically reducing the throat area, used as a surge resistance technique, improved the quality of surge resistance by 12%, with a minor loss of efficiency of less than 2%. Experimental studies of variable-throat diffusers have been done by Filipenco et al. [21]. They determined that active control of the throat increased the level of stabilization, thereby expanding the operational range by 14%, while maintaining efficiency within ±1.5 percent of baseline levels. Simon et al. [22] have investigated the synchronous optimization of inlet guide vanes and diffuser vanes, achieving an efficiency performance of 5% and a 7% increase in pressure ratio. Jawad researched wedge-shaped diffuser blades [23], which resulted in an additional 20% increase in the compressor's operational range through an improved pressure ratio of up to 6% and enhanced stability potential. In a comparative study of Vaneless and vaned diffusers based on CFD, Jawad et al. [24] found that vaneless diffusers improved the efficiency by 4% under changing conditions. In comparison, regarding vaned diffusers, the improvement reached 6% at high and constant flow. Hamel et al. [25] considered new designs for volutes which allowed for a better distribution of flow, resulting in energy losses reduced by almost 8%, especially at off-design operation, therefore increasing system reliability. Watson and Janota [26] designed a hydraulic actuation system for VGTs. They saw a 30% reduction in response time over a 12% change (+/-12%) in system weight (more) compared to traditional pneumatic actuators. Laghrouche et al. [27] proposed nonlinear control algorithms for pneumatic actuators, which improved the transient stability of the output by 22% in terms of overshoot reduction and increased robustness against load variations by 15%.

Shirakawa et al. [28] presented a cooperative control strategy for VGT and EGR, which improved system response, resulting in a reduction of almost 25% in turbo lag and a decrease of 28% in NOx emissions compared to traditional methods. El Hameur et al. [29] reported the vortex dynamics in centrifugal compressors using CFD. They demonstrated that the losses produced by the vortices accounted for approximately 10% of the efficiency loss and that secondary flows accounted for a change in energy losses of almost 7% of the total energy losses. Liu et al. [30] examined the effects of vane angle variation using the CFD method, which revealed that the optimal value of vane angle position could provide a 9% increase in pressure ratio and approximately a 12% delay in stall inception within the flow range. Sabahi et al. [31] presented work on advanced nozzle geometries in turbocharger turbines, concluding that the various flow incidence angles resulted in a 5% efficiency gain and 7% increased work output of the turbines. Heidary et al. [32] studied compressor surge performance using CFD analysis, and the findings confirmed that VGT could provide a surge margin improvement of approximately 20% and stabilize pressure oscillations by 18% of the pressure fluctuations at the transient level.

Despite the elevated level of knowledge on the VGT mechanisms, there are knowledge gaps. First, many investigations focus on turbine side geometry variations or compressor side geometry variations; less attention is given to the combined effect of variable geometry on both members. Second, although many studies have been conducted where efficiencies improved, there has been no systematic research on various operating conditions, such as different inlet angles, rotational speeds, and expansion ratios (ERs), which can be important for practical engine cycles. Third, although control strategies of VGTs have become increasingly sophisticated, research regarding the dynamical performance of VGT actuation in transient regimes has not investigated its effects on the aerodynamic performance of VGTs.

This study attempts to fill the gaps in the understanding of centrifugal compressors in integrated VGT systems using CFD analysis. It includes making some geometry using Vista RTD and BladeGen, meshing using TurboGrid, and performing computations using ANSYS CFX. The research examines compressor performance for various inlet angles (50°, 60°, 70°), rotational speeds (30,000 to 90,000 rpm), and ERs (1.6 to 2.8). The use of a mesh independence study improves the numerical accuracy. The aim is to provide an understanding of the correlations between geometry, flow control, and efficiency for optimizing next-generation VGT systems.

This paper presents a CFD-based analysis of a radial turbine under various conditions, examining the effects of inlet angle, ER, and speed. It highlights the relationship between flow behavior and efficiency, offering practical recommendations for turbine design and VGT optimization.

2. METHODOLOGY

2.1 Geometric model

A radial turbine has been designed based on the given mean-line parameters using ANSYS 2021 R1. An impeller with a shroud exducer radius ratio of 0.66, a hub exducer radius ratio of 0.29, or an axial length to diameter ratio of 0.40 was used. It was based on a design having 15 vanes, a mean exit thickness of 0.8 mm, and a relative tip clearance height of 0.04. A radial stacking law was employed, and the vane surface finish was specified as "cast" to accommodate realistic manufacturing tolerances. The mean line design is shown in Figure 1, and the basic parameters are shown in Table 1. The geometry was then transferred into the ANSYS BladeGen, where three-dimensional models of the impeller and vanes were designed, as shown in Figure 2. Trailing edge angles, blade stacking, etc., were all studied to render it practicable both to manufacture and in terms of its aerodynamics.

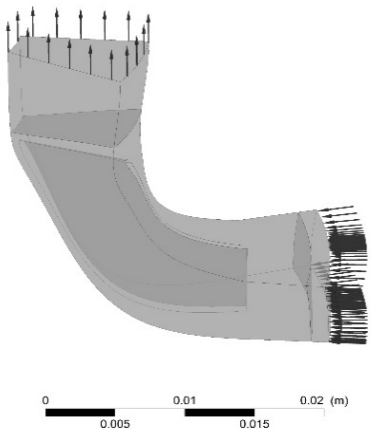

Figure 1. Mean-line design of the radial turbine in ANSYS

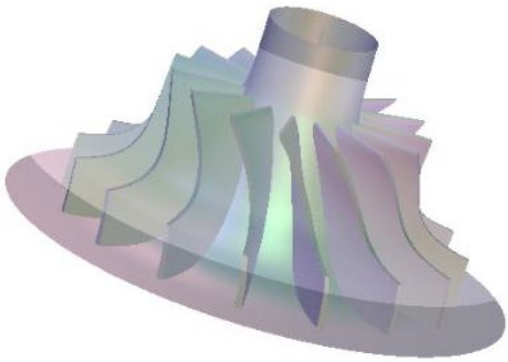

Figure 2. Three-dimensional impeller and vane geometry generated in ANSYS

Table 1. Geometric parameters of the radial turbine

Parameter	Value	Notes
Shroud exducer radius ratio	0.66	From Vista RTD
Hub exducer radius ratio	0.29	From Vista RTD
Axial length/diameter ratio	0.40	Specified
Number of vanes	15	
Vane thickness at exit	0.8 mm	Mean value
Tip clearance ratio	0.04	Relative to blade span
Spanwise stacking law	Radial	

2.2 Governing equations

The flow field is modeled by employing the incompressible Reynolds-averaged Navier-Stokes (RANS) equations. The governing conservation equations are presented as:

Continuity equation:

$$\rho\left(\nabla\vec{V}\right)=0 \tag{1}$$

Momentum equation:

$$\rho\,\nabla\vec{V}^2=-\nabla P+\mu\nabla^2\vec{V} \tag{2}$$

Energy equation:

$$\rho C_P\left(\vec{\mathrm{V}}\,\nabla\mathrm{T}\right)=K\nabla^2T \tag{3}$$

where, V is the velocity vector, ρ is the air density, $\vec{V}$ is the velocity vector, P is the pressure, T is the temperature, C_P is the specific heat, and K is the thermal conductivity.

The standard k–ε model uses the following transport equations for k and ε.

Turbulence kinetic energy (k):

$$\frac{\partial(\rho uk)}{\partial x}+\frac{\partial(\rho vk)}{\partial y}+\frac{\partial(\rho wk)}{\partial z}=\frac{\partial}{\partial x}\left(\frac{\mu_t}{\sigma_k}\frac{\partial k}{\partial x}\right)+\frac{\partial}{\partial y}\left(\frac{\mu_t}{\sigma_k}\frac{\partial k}{\partial y}\right)+\frac{\partial}{\partial z}\left(\frac{\mu_t}{\sigma_k}\frac{\partial k}{\partial z}\right)+P_k+G_k-\rho\varepsilon \tag{4}$$

Dissipation rate (ε):

$$\frac{\partial(\rho u\varepsilon)}{\partial x}+\frac{\partial(\rho v\varepsilon)}{\partial y}+\frac{\partial(\rho w\varepsilon)}{\partial z}=\frac{\partial}{\partial x}\left(\frac{\mu_t}{\sigma_\varepsilon}\frac{\partial\varepsilon}{\partial x}\right)+\frac{\partial}{\partial y}\left(\frac{\mu_t}{\sigma_\varepsilon}\frac{\partial\varepsilon}{\partial y}\right)+\frac{\partial}{\partial z}\left(\frac{\mu_t}{\sigma_\varepsilon}\frac{\partial\varepsilon}{\partial z}\right)+C_{1\varepsilon}\frac{\varepsilon}{k}(P_k+G_k)-C_{2\varepsilon}\rho\frac{\varepsilon^2}{k} \tag{5}$$

where, σ_k is the turbulent Prandtl number of k, and σ_ε is the turbulent Prandtl number of ε.

$$P_k=\mu_t\left(2\left[\left(\frac{\partial u}{\partial x}\right)^2+\left(\frac{\partial v}{\partial y}\right)^2+\left(\frac{\partial w}{\partial z}\right)^2\right]+\left(\frac{\partial u}{\partial x}+\frac{\partial u}{\partial y}+\frac{\partial u}{\partial z}\right)^2\right) \tag{6}$$

$$G_k=\frac{\mu_t}{\sigma_t}g\beta\frac{\partial T}{\partial y} \tag{7}$$

where, G_k is the kinetic energy generated by buoyancy.

Turbulence closure was achieved using the k-ε model because of its established effectiveness in turbomachinery simulations. The related transport equations for turbulent kinetic energy (k) and dissipation rate (ε) were solved concurrently.

Table 2 outlines the boundary conditions utilized in the simulations. A uniform velocity is specified at the inlet, while a constant static pressure is maintained at the outlet. No-slip conditions are enforced at all solid walls, and a rotational periodicity is established at the interface between adjacent blade passages. The thermophysical properties of the working fluid (air) are detailed in Table 3.

2.3 Mesh generation

The computational space was discretised by a regular hexahedral structured mesh generated in ANSYS TurboGrid.

An O-grid formulation was used near the leading and trailing edges of the blade to resolve the boundary layer flow and effectively reduce the skewness. A smaller mesh size was used in the area of higher curvature to capture phenomena such as flow separation and secondary flow precisely. Near-wall resolution was controlled to maintain a value of y+ less than 1.0, ensuring that the viscous sublayer was resolved entirely and eliminating the need for wall functions. The representative distributions of the meshes are illustrated in Figures 3 and 4. A mesh-independent result was obtained by validating five grid densities corresponding to approximately 0.25 million, 0.45 million, 0.95 million, 1.45 million, and 2.0 million elements. The variable tracked for independence was shaft power, reflecting compressor efficiency and aerodynamic losses. Results in Figure 5 indicate that predictions become steady after approximately 1.45 million elements, which varies less than 0.5% from the densest grid. Therefore, a grid size of roughly 1.45 million elements was employed for all subsequent simulations, representing a compromise between the trade-off between computational costs and precision.

Table 2. Operating boundary conditions applied in the CFD simulations

Boundary Condition	Specification	Notes
Inlet total temperature	1000 K	Fixed for all cases
Inlet total pressure	Varied (1.6–2.8 bar)	To achieve ER = 1.6–2.8
Outlet static pressure	Adjusted	Matches the desired expansion ratio
Rotational speed	30,000; 60,000; 90,000 rpm	Three operating speeds
Inlet flow angle (α)	50°, 60°, 70°	Absolute inlet flow angle
Working fluid	Ideal gas (air)	γ = 1.4, R = 287 J/kg·K

Table 3. Thermophysical properties of the working fluid (air) at reference conditions

Property	Value	Notes
Specific heat (Cp)	1007 J/kg·K	At 300 K
Ratio of specific heats (γ)	1.4	Ideal gas assumption
Gas constant (R)	287 J/kg·K	Universal relation R = Cp – Cv
Dynamic viscosity (μ)	1.8×10^{-5} Pa·s	Constant with temperature
Thermal conductivity (k)	0.026 W/m·K	At 300 K

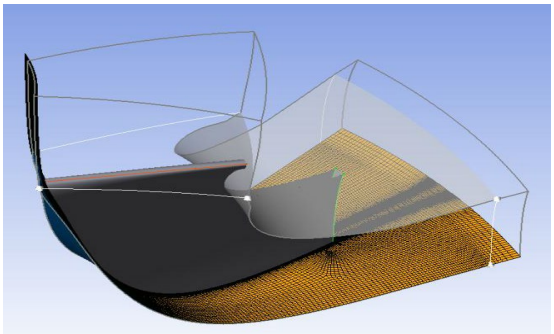

Figure 3. Structured mesh of the computational domain generated in ANSYS

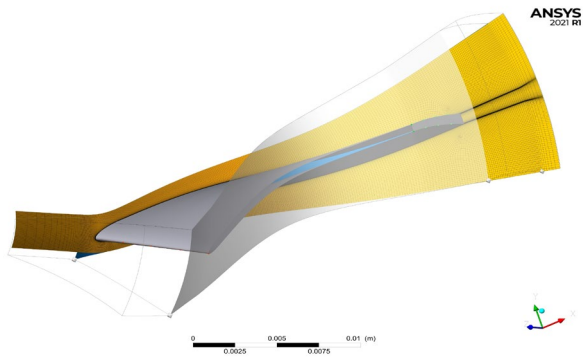

Figure 4. O-grid topology to the leading/ trailing edges of the blade

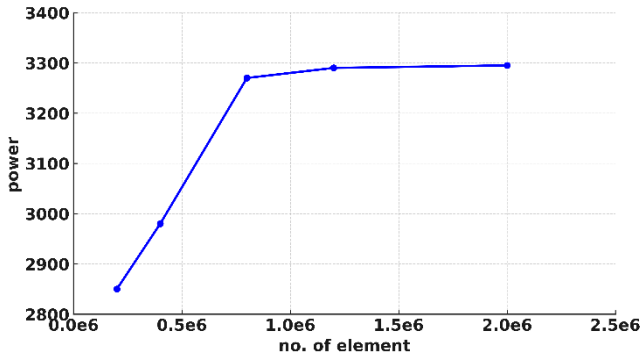

Figure 5. Mesh Independence test: Power as a function of the number of elements

3. RESULTS AND DISCUSSION

This part shows the numerical results and performance analysis of the radial inflow turbine. In general, the influences of ER, rotational speed, and inlet angle on the output power, efficiency, and comprehensive energy recovery were investigated. The thermodynamic and aerodynamic characteristics of the entire system for various ER and rotational speeds are presented in Figures 6-9. The performance map below, in Figure 6, clearly illustrates the dependencies on ER and speed. For an ER value of 1.6, efficiency can be increased from 0.26 at 30,000 rpm to 0.63 at 90,000 rpm, representing an approximately 142% increase in efficiency. However, for ER values above 2.4, the benefits drop off, and the levels of efficiency approach 0.45–0.47. This plateau is a good indication that there is an optimum range of operation, with further increase in ER showing only a marginal increase due to the rise in aerodynamic losses and irreversibility of heat addition.

Figure 7 shows the dependence of ER and output power as a function of circumferential inlet angle (a = 50°, 60°, and 70°) for a wide range of speeds (30,000–90,000 rpm). At an inlet angle of a = 50°, the lowest power levels are observed, ranging from 259 W at ER = 1.2 to 702 W at ER = 2.2 at 30000 rpm, representing an increase of 171%. This power output continues to increase at higher rotational speeds, rising from 178 W to 1214 W at 90,000 rpm, a 582% improvement. The power output reveals a more even rise in power with an increasing inlet angle, with a peak power reaching 2,671 W at an inlet angle of 90,000 rpm, representing a 130% power increase for the lowest ER. The best performance appears to be achieved

at a = 70 deg, with a power increase from 1,358 to 3,286 at 90,000 rpm, corresponding to a 142% increase. In comparison, the output power for a = 70 is about three times greater than the output power for a = 50 for the same conditions. These results validate the fact that both ER and rotational speed play a significant role in the performance of the expander. Furthermore, the inlet angle is optimized to maximize energy extraction, and the optimal balance of flow stability and work recovery is achieved at an angle of 70°. Variation of outlet pressure against ER is presented in Figure 8. At 30,000 rpm, this increase is 66% for ER = 1.6 - it would correspond to a pressure of 1.38 bar, and for ER = 2.8, that would be 2.29 bar. Similar trends are noted with 60,000 rpm (1.34 to 2.22 bar) and 90,000 rpm (1.31 to 2.10 bar). While the percent increase of outlet pressure is the same as any other rpm value, the actual pressure values show lower pressure at high rpm, which hints at another aerodynamic loss that prevents the formation of high pressure at high rpm. The pressure ratio in Figure 9, on the other hand, has a different behavior. Where the order is 30,000 rpm, the corresponding relative pressure ratio decreases from 0.86 at ER = 2.0 to 0.79 at ER = 2.8. At 90,000 rpm, this speed drops from 0.73 to 0.69, indicating a roughly 13–15% decrease in speed within the range of ERs studied. This phenomenon suggests that distortions of the internal flow and thermal irreversibility occur to prevail over the increase in effective compressive capability, just as the increase in outlet pressure and power output occurs when attempting higher speeds.

Overall, Figures 6-9 illustrate a significant trade-off among efficiency, pressure behavior, and power generation. Although increasing the ER and rpm significantly increases the output power (by as much as 582%) and outlet pressure (by as much as 66%), there is a corresponding decrease in pressure ratio and efficiency gain. This is considered to provide the best balance when ER values of 2.4 to 2.8 are used, along with rotational speeds of 60,000 to 90,000 rpm. This analysis draws attention to the fact that there is no infinite power and efficiency capability, and that it also has to consider compromises when it comes to the pressure ratio as well.

The results show that, in the case of applying micro-turbines, Organic Rankine Cycle (ORC) expanders, and power recovery systems with small scale, it is recommended to have ERs and rotational speeds at mid-high values. This approach is seen to offer a favorable combination of performance and pressure stability simultaneously. Operating at too fast a speed may be the most effective way to increase power outputs; however, this comes at the expense of system stability and longevity. This makes it essential to take great care in selecting the operating conditions during the design phase to account for the real world.

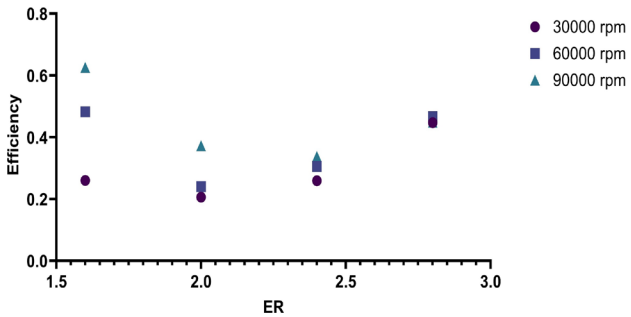

(a)

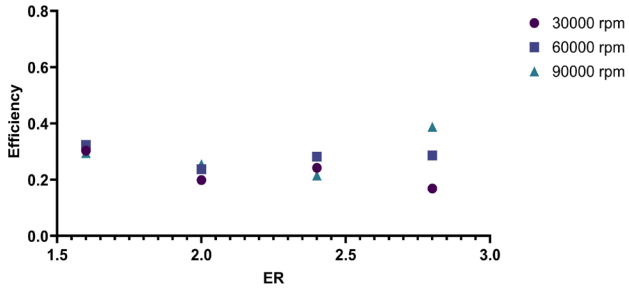

(b)

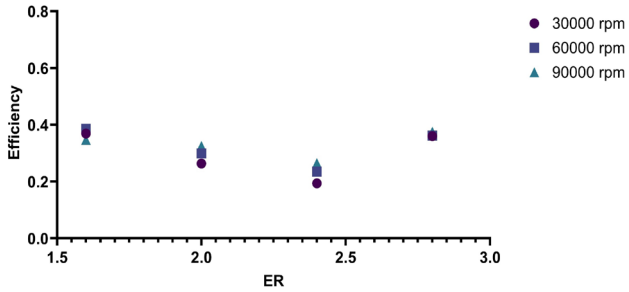

(c)

Figure 6. Variation of expander efficiency with expansion ratio at (a) α = 50°, (b) α = 60°, and (c) α = 70°

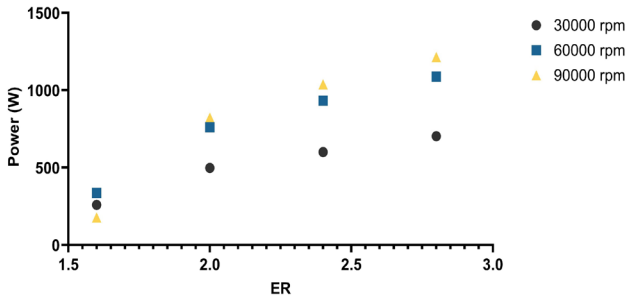

(a)

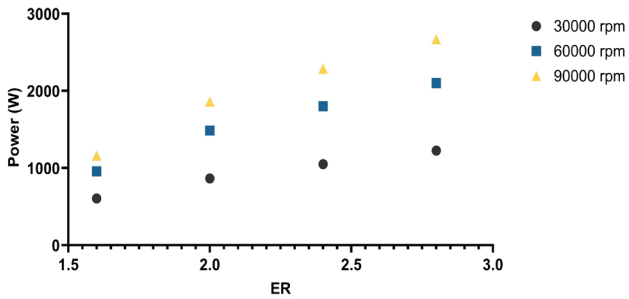

(b)

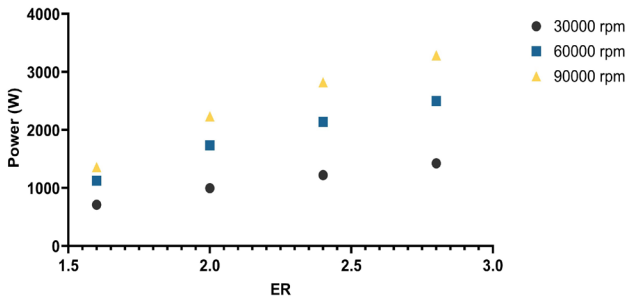

(c)

Figure 7. Variation of output power with expansion ratio at (a) α = 50°, (b) α = 60°, and (c) α = 70°

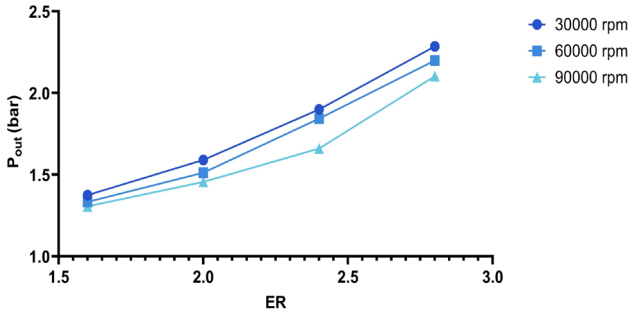

(a)

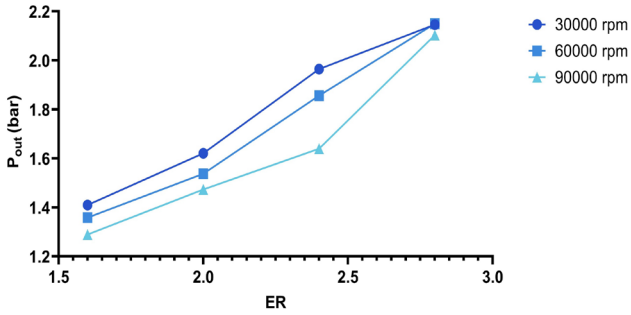

(b)

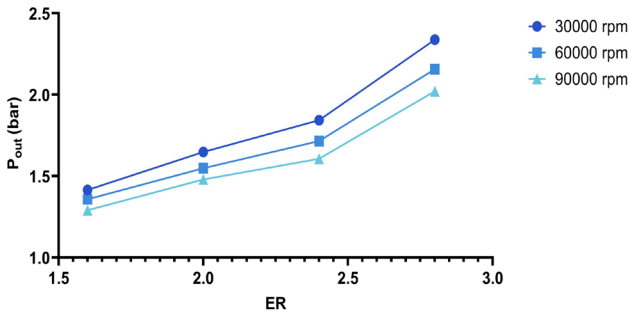

(c)

Figure 8. Variation of total outlet pressure with expansion ratio at (a) α = 50°, (b) α = 60°, and (c) α = 70°

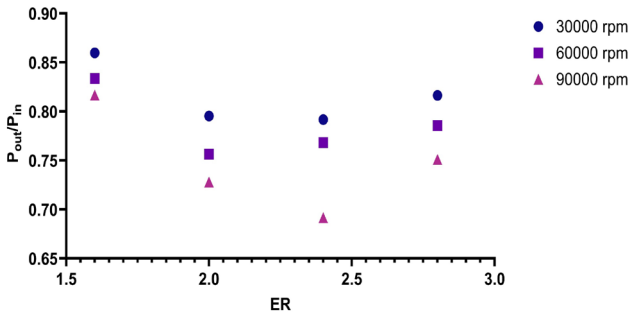

(a)

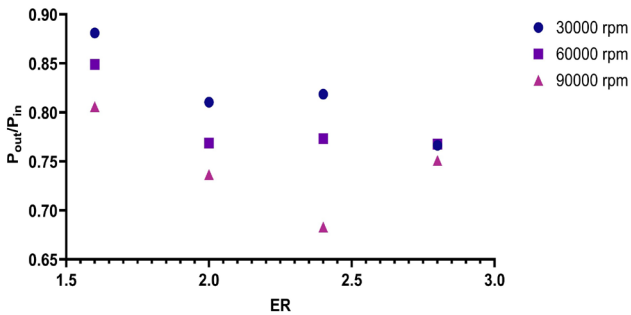

(b)

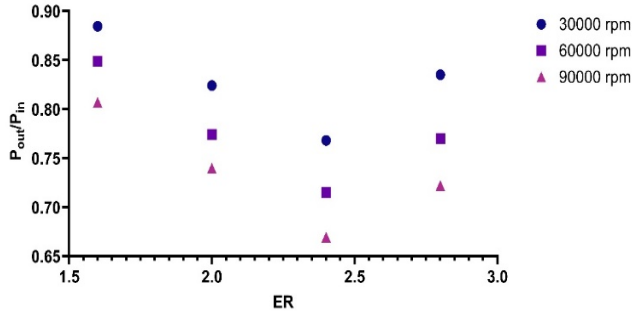

(c)

Figure 9. Variation of pressure ratio with expansion ratio at (a) α = 50°, (b) α = 60°, and (c) α = 70°

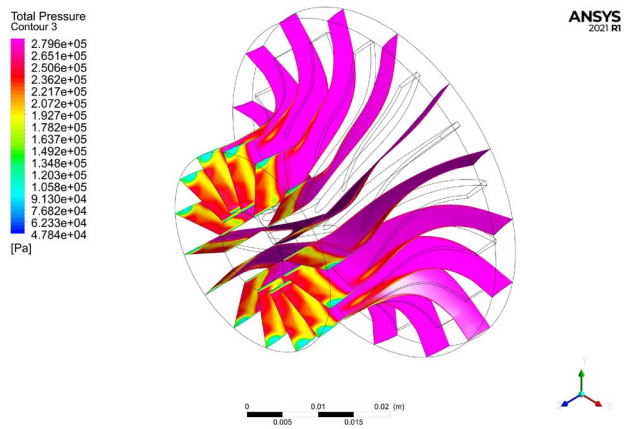

(a)

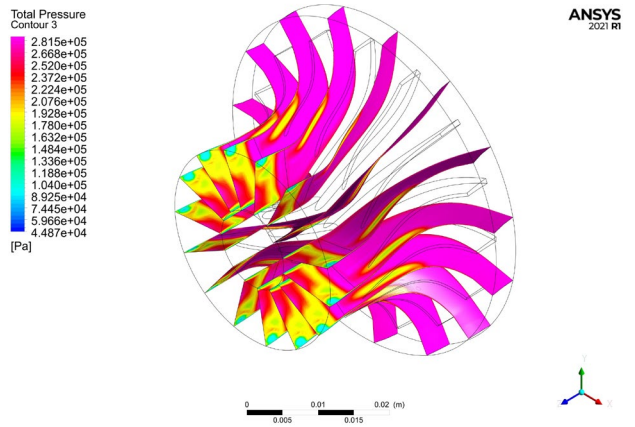

(b)

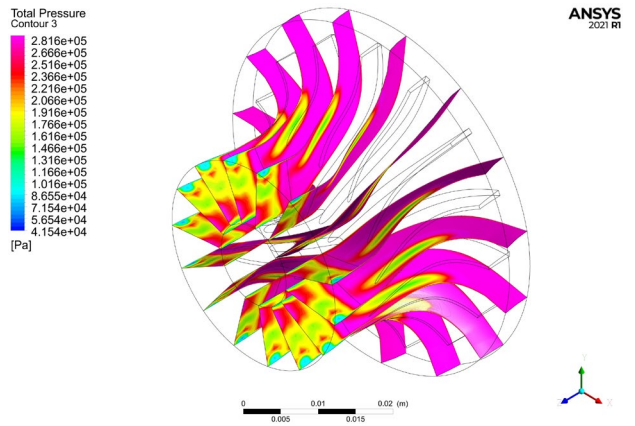

(c)

Figure 10. Pressure contours within the expander at (a) 30,000 rpm, (b) 60,000 rpm, and (c) 90,000 rpm

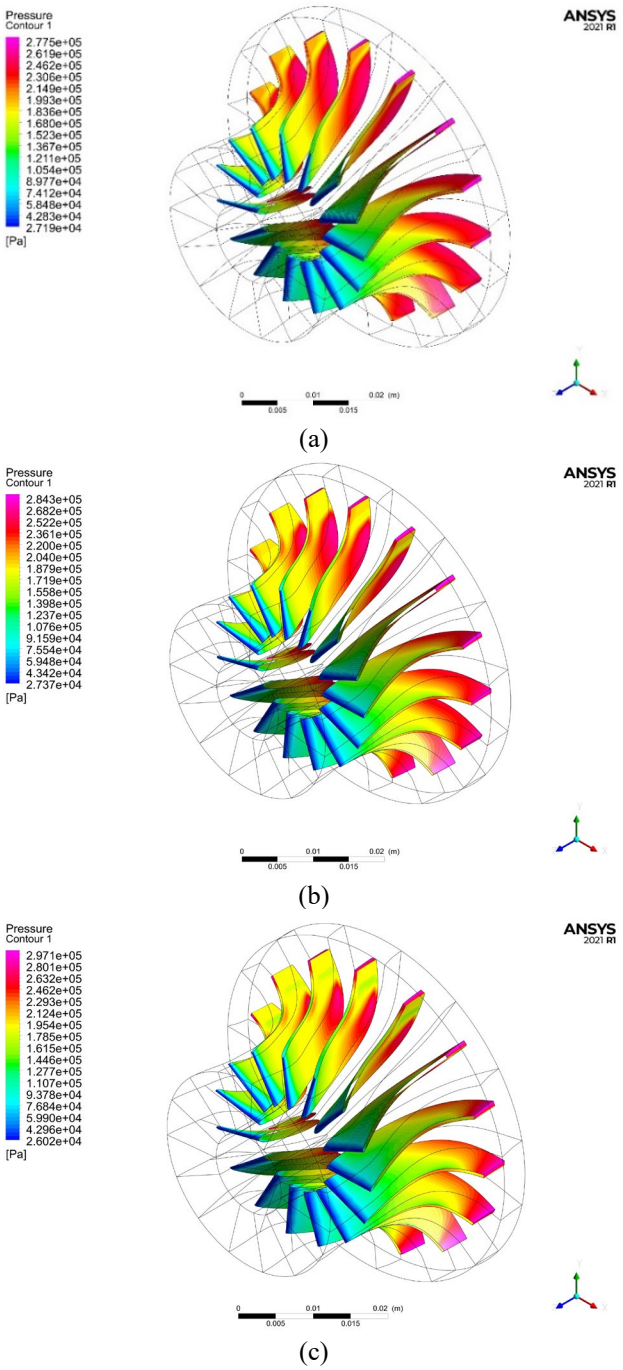

Figure 11. Blade surface pressure distribution across suction and pressure sides at (a) 30,000 rpm, (b) 60,000 rpm, and (c) 90,000 rpm

The pressure distribution given in Figure 10 shows that as the rotor speed is increased, so does the pressure drop across the expander. At a speed of 30000 rpm, the difference between the pressure inside the inlet and on the outlet was 0,12 MPa. At 60,000 rpm, however, this pressure drop was 0.24 MPa, a 100% difference. The trend continued at 90,000 rpm, resulting in a pressure drop of 0.36 MPa, approximately 200% higher than the lowest speed. This trend is also evident in the blade surface pressure distributions shown in Figure 11, which indicate that the pressure on the suction side decreases from 0.92 MPa at 30,000 rpm to 0.78 MPa at 90,000 rpm. 15% in differences. On the other hand, the pressure side was found to be consistently greater than 1.1 MPa, which corresponds to high aerodynamic loading and high torque through the shaft at high speeds. Figure 12 shows that increasing rotational speed raises the local Mach number, especially near the blade leading edge and suction side. At 90,000 rpm, stronger compressibility effects appear, causing higher losses and explaining the slight drop in efficiency at high speed.

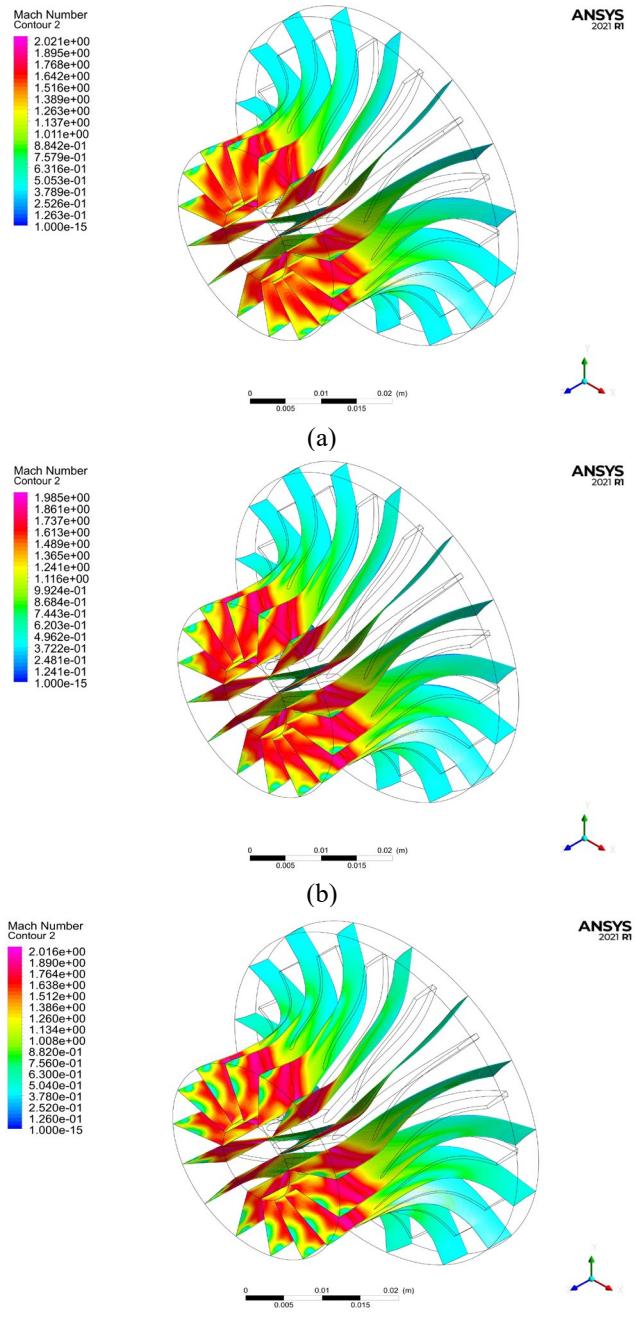

Figure 12. Mach number distribution along the flow passage at (a) 30,000 rpm, (b) 60,000 rpm, and (c) 90,000 rpm

Comparatively, in terms of isentropic efficiency, the value at 30,000 rpm was 61%, as shown in Figure 13. At the higher revolution of 60,000 rpm, efficiency improved considerably, reaching 73 percent (almost 20 percent more). At 90,000 rpm, however, the efficiency was 69%, which was 5% less than optimum efficiency. This reduction has been attributed to the development of secondary flows, mixing losses, and vortical structures, which counter the benefits of the increased pressure ratios. These observations suggest that maximum aerodynamic efficiency occurs at 60,000 rpm, where the averaging out of the effects of compressibility begins to show

its impact on performance.

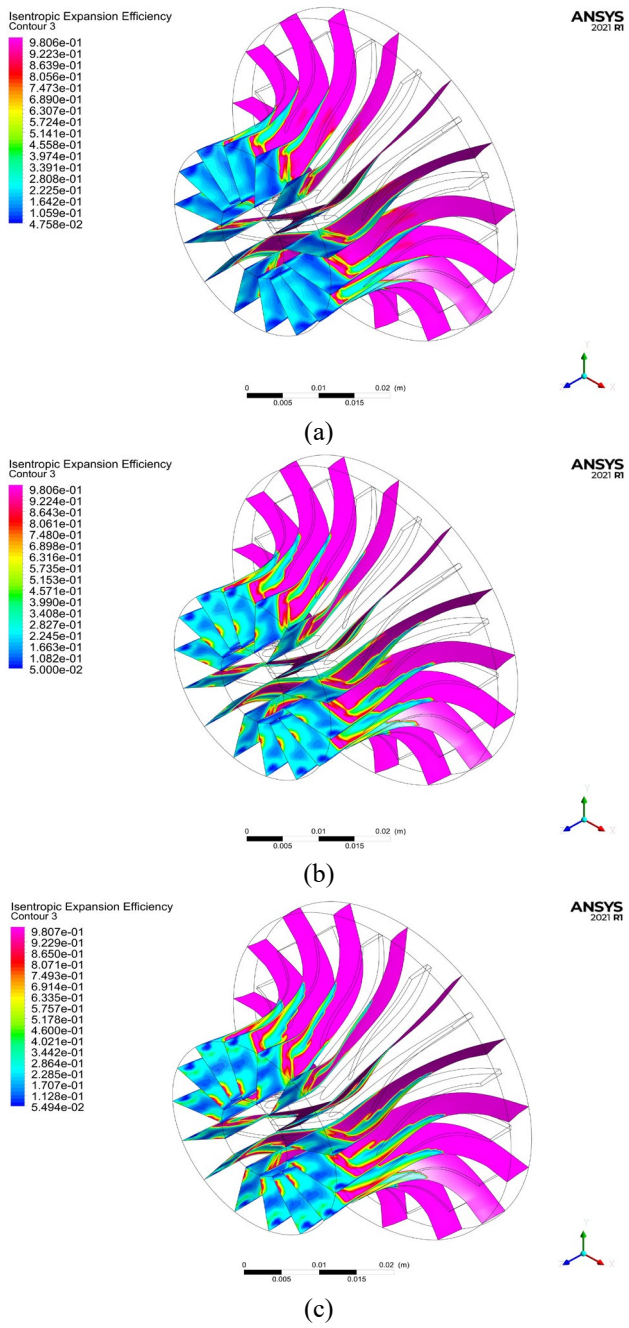

Figure 13. Isentropic efficiency contour of the expander at (a) 30,000 rpm, (b) 60,000 rpm, and (c) 90,000 rpm

The velocity vectors in Figure 14 are also consistent with these results. The maximum speed was 95 meters per second at a 30,000 rpm speed, which increased to 155 meters per second at a 60,000 rpm speed - a 63% increase. At the speed of 90,000 rpm, the speed increased 121% from 30 thousand rpm to 210 m/s. However, this increase is accompanied by an increase in the area of recirculation regions near the hub and trailing edge of the wings, indicating flow separation and the production of turbulence. As a result, there is a slight degradation in efficiency at the maximum velocity.

In conclusion, by aggregating the results obtained, it is evident that the combination of the 60,000 rpm expander and the 30,000 rpm expander yields a favorable ratio of pressure rise, velocity gain, and increase in Mach number, which can potentially result in a 20% increase in efficiency. However, by increasing the speed to 90 thousand rpm, the pressure drop is increased (200% pressure drop), the velocities are increased (121%), as well as the flow instabilities appear, and the efficiency decreases (5% from the optimal condition). Thus, the optimum operating condition for the expander to operate smoothly and efficiently is confirmed to be 60,000 rpm.

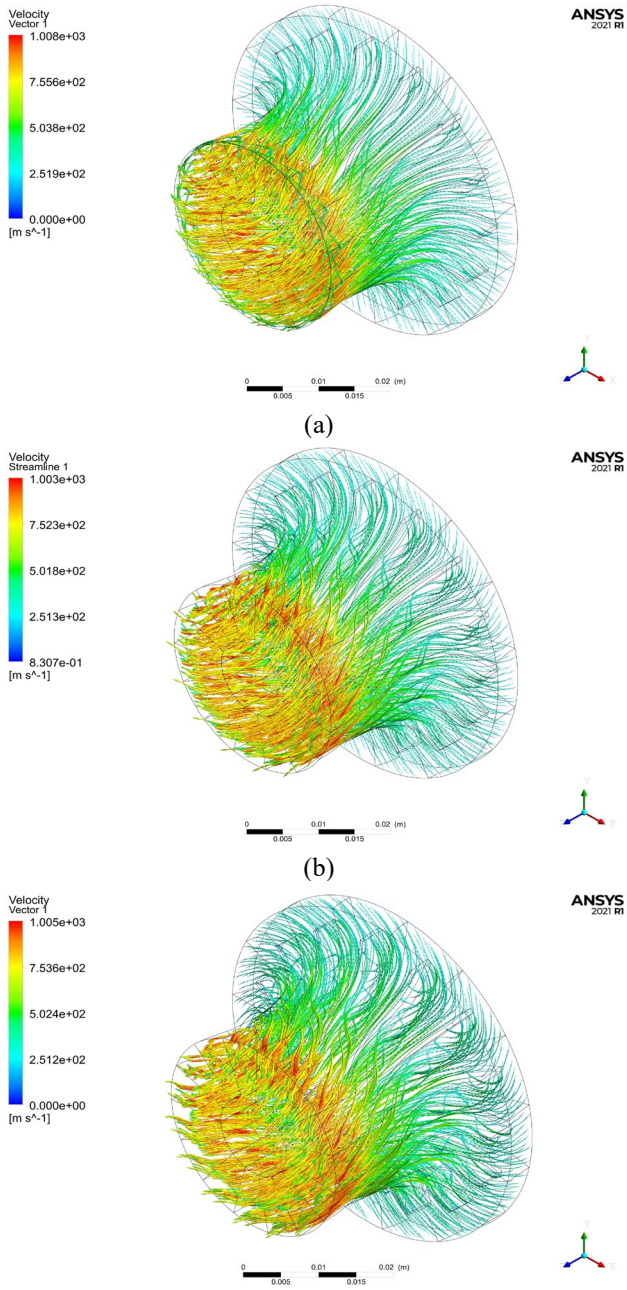

Figure 14. Velocity vector distribution within the expander at (a) 30,000 rpm, (b) 60,000 rpm, and (c) 90,000 rpm

Future studies could be conducted to extend the current CFD analysis to a stage where different turbulence models are compared, and the effect of the model on prediction accuracy is tested. Additionally, transient simulations can be made to determine the effects of unsteady flow and dynamic performance behavior. Experimental validation under various operating conditions would also enhance confidence in the numerical results and support further optimization of radial turbine design.

4. CONCLUSION

This work shows a detailed CFD study of a radial turbine with different inlet angles, ERs, and rotational speeds. The results of the analysis showed that the turbine's performance is primarily determined by the effects of the container's speed and ER, which have a direct impact on the flow structure and efficiency. As the increase in speed was brought about, the efficiency was markedly increased, but began to flatten at the higher ERs because of increasing aerodynamic and thermal losses.

Optimum performance has been achieved at around 60,000 rpm and an ER as high as 2.4–2.8, where efficiency, outlet pressure, and power output were in a favorable balance, given the ER. At higher speeds (90,000 rpm), higher velocity gradients and recirculation areas were observed close to the blade suction side, leading to lower efficiency and some flow instability. It was also found that power generation was sensitive to the inlet flow angle, with a flow angle of 70 deg found to be the most balanced compromise between performance and stability.

The experiment results show that, although higher speeds and ERs improve power output and pressure, they also increase the losses that scale with these variables, which in turn reduce efficiency. Flow field visualization confirmed that pressure gradients and local turbulence have a significant effect on the energy conversion.

Overall, this work provides a deeper understanding of the flow-geometry-performance behavior in radial turbines and is of great value in optimizing the applications of micro-turbines and ORC expanders. Future research will include a comparison of the different types of turbulence models, transient simulations, and experimental validation towards an improved predictive capability and advancement of still unrealized turbine designs.

REFERENCES

[1] Nyongesa, A.J., Park, M.H., Lee, C.M., Choi, J.H., Pham, V.C., Hur, J.J., Lee, W.J. (2024). Experimental evaluation of the significance of scheduled turbocharger reconditioning on marine diesel engine efficiency and exhaust gas emissions. Ain Shams Engineering Journal, 15(8): 102845. https://doi.org/10.1016/j.asej.2024.102845

[2] Helmers, E., Leitão, J., Tietge, U., Butler, T. (2019). CO_2-equivalent emissions from European passenger vehicles in the years 1995–2015 based on real-world use: Assessing the climate benefit of the European "diesel boom". Atmospheric Environment, 198: 122-132. https://doi.org/10.1016/j.atmosenv.2018.10.039

[3] Reitz, R.D., Ogawa, H., Payri, R., Fansler, T., et al. (2019). IJER editorial: The future of the internal combustion engine. International Journal of Engine Research, 21(1): 3-10. https://doi.org/10.1177/1468087419877990

[4] Leduc, P., Dubar, B., Ranini, A., Monnier, G. (2003). Downsizing of gasoline engine: An efficient way to reduce CO2 emissions. Oil & Gas Science and Technology, 58(1): 115-127. https://doi.org/10.2516/ogst:2003008

[5] Hu, B., Akehurst, S., Brace, C. (2015). Novel approaches to improve the gas exchange process of downsized turbocharged spark-ignition engines: A review. International Journal of Engine Research, 17(6): 595-618. https://doi.org/10.1177/1468087415599866

[6] Feneley, A.J., Pesiridis, A., Andwari, A.M. (2017). Variable geometry turbocharger technologies for exhaust energy recovery and boosting-A review. Renewable and Sustainable Energy Reviews, 71: 959-975. https://doi.org/10.1016/j.rser.2016.12.125

[7] Kalghatgi, G., Johansson, B. (2018). Gasoline compression ignition approach to efficient, clean and affordable future engines. Proceedings of the Institution of Mechanical Engineers, part D: Journal of Automobile Engineering, 232(1): 118-138. https://doi.org/10.1177/0954407017694275

[8] Rakopoulos, C.D., Giakoumis, E.G. (2004). Availability analysis of a turbocharged diesel engine operating under transient load conditions. Energy, 29(8): 1085-1104. https://doi.org/10.1016/j.energy.2004.02.028

[9] Moulin, P., Chauvin, J. (2011). Modeling and control of the air system of a turbocharged gasoline engine. Control Engineering Practice, 19(3): 287-297. https://doi.org/10.1016/j.conengprac.2009.11.006

[10] Galloway, L., Kim, S.I., Park, J., Kwon, S., Yoo, S. (2021). Aerodynamic design optimization of a variable geometry nozzle vane for automotive turbochargers. In Proceedings of the ASME Turbo Expo 2021: Turbomachinery Technical Conference and Exposition. Volume 2C: Turbomachinery — Design Methods and CFD Modeling for Turbomachinery; Ducts, Noise, and Component Interactions. Virtual, Online, p. V02CT34A032. https://doi.org/10.1115/GT2021-59616

[11] Asanaka, Y., Nishimura, R., Miyagwa, K., Yoshida, T., Ebisu, M. (2022). Influence of nozzle clearance of VG turbocharger turbine on performance and internal flow. Journal of Physics: Conference Series, 2217: 012084. https://doi.org/10.1088/1742-6596/2217/1/012084

[12] Danlos, A., Podevin, P., Deligant, M., Clenci, A., Punov, P., Guilain, S. (2022). Turbocharger surge behavior for sudden valve closing downstream of the compressor and the effect of actuating a variable nozzle turbine. IOP Conference Series: Earth and Environmental Science, 960: 012013. https://doi.org/10.1088/1755-1315/960/1/012013

[13] Gupta, B., Yoshida, T., Ogawa, S., Danmoto, Y., Yoshimoto, T. (2021). Improving Vibration response of radial turbine in variable geometry turbochargers with CFD analysis. In Proceedings of the ASME Turbo Expo 2021: Turbomachinery Technical Conference and Exposition. Volume 6: Ceramics and Ceramic Composites; Coal, Biomass, Hydrogen, and Alternative Fuels; Microturbines, Turbochargers, and Small Turbomachines. Virtual, Online, p. V006T19A009. https://doi.org/10.1115/GT2021-59139

[14] Lee, B., Jung, D., Assanis, D., Filipi, Z. (2008). Dual-stage turbocharger matching and boost control options. In Proceedings of the ASME 2008 Internal Combustion Engine Division Spring Technical Conference. ASME 2008 Internal Combustion Engine Division Spring Technical Conference. Chicago, Illinois, USA, pp. 267-277. https://doi.org/10.1115/ICES2008-1692

[15] Stefanopoulou, A.G., Kolmanovsky, I., Freudenberg, J.S. (2002). Control of variable geometry turbocharged diesel engines for reduced emissions. IEEE Transactions on Control Systems Technology, 8(4): 733-745.

https://doi.org/10.1109/87.852917
[16] Zhao, B., Zhao, Q.J., Zhao, W., Xiang, X.R., Zhou, X.Y. (2020). Numerical and experimental investigation of turbocharger compressor low-end performance improvement using a variable geometry inlet orifice. International Journal of Engine Research, 22(8): 2492-2501. https://doi.org/10.1177/1468087420951097
[17] Tamaki, H., Yamaguchi, S. (2024). A method for preliminary design of variable geometry vaned diffuser for centrifugal compressor. Journal of Turbomachinery, 146(3): 031014. https://doi.org/10.1115/1.4064083
[18] Ludtke, K. (1983). Aerodynamic tests on centrifugal process compressors—The influence of the vaneless diffusor shape. Journal of Engineering for Gas Turbines and Power, 105(4): 902-909. https://doi.org/10.1115/1.3227499
[19] Whitfield, A., Wallace, F.J., Atkey, R.C. (1976). The effect of variable geometry on the operating range and surge margin of a centrifugal compressor. In Proceedings of the ASME 1976 International Gas Turbine and Fluids Engineering Conference. Volume 1B: General. New Orleans, Louisiana, USA, p. V01BT02A033. https://doi.org/10.1115/76-GT-98
[20] Abdelhamid, A.N. (1982). Control of self-excited flow oscillations in vaneless diffuser of centrifugal compression systems. In Proceedings of the ASME 1982 International Gas Turbine Conference and Exhibit. Volume 1: Turbomachinery. London, England, p. V001T01A065. https://doi.org/10.1115/82-GT-188
[21] Filipenco, V.G., Deniz, S., Johnston, J.M., Greitzer, E. M., Cumpsty, N.A. (1998). Effects of inlet flow field conditions on the performance of centrifugal compressor diffusers: Part 1 — Discrete-passage diffuser. In Proceedings of the ASME 1998 International Gas Turbine and Aeroengine Congress and Exhibition. Volume 1: Turbomachinery. Stockholm, Sweden, p. V001T01A111. https://doi.org/10.1115/98-GT-473
[22] Simon, H., Wallmann, T. Mo¨nk, T. (1987). Improvements in performance characteristics of single-stage and multistage centrifugal compressors by simultaneous adjustments of inlet guide vanes and diffuser vanes. Journal of Turbomachinery, 109(1): 41-47. https://doi.org/10.1115/1.3262068
[23] Jawad, L.H., Abdullah, S., Zulkifli, R., Mahmood, W.M.F.W. (2012). Modelling of centrifugal compressor impellers using adaptive neuro-fuzzy inference systems (ANFIS). International Review of Mechanical Engineering, 6(5): 1011.
[24] Jawad, L.H., Abdullah, S., Zulkifli, R., Mahmood, W.M.F.W. (2014). Numerical study on the effect of interaction vaned diffuser with impeller on the performance of a modified centrifugal compressor. Journal of Mechanics, 30(2): 113-121. https://doi.org/10.1017/jmech.2013.49
[25] Hamel, M., Hamidou, M.K., Cherif, H.T., Abidat, M., Litim, S.A. (2008). Design and flow analysis of radial and mixed flow turbine volutes. In Proceedings of the ASME Turbo Expo 2008: Power for Land, Sea, and Air. Volume 6: Turbomachinery, Parts A, B, and C. Berlin, Germany, pp. 2329-2338. https://doi.org/10.1115/GT2008-50503
[26] Watson, N., Janota, M.S. (1982). Turbocharging the Internal Combustion Engine. Bloomsbury Academic. https://doi.org/10.1007/978-1-349-04024-7
[27] Laghrouche, S., Mehmood, A., El Bagdouri, M. (2012). Study of the nonlinear control techniques for single acting VGT pneumatic actuator. International Journal of Vehicle Design, 60(3/4): 264-285. https://doi.org/10.1504/IJVD.2012.050084
[28] Shirakawa, T., Itoyama, H., Miwa, H. (2001). Study of strategy for model-based cooperative control of EGR and VGT in a diesel engine. JSAE Review, 22(1): 3-8. https://doi.org/10.1016/S0389-4304(00)00100-4
[29] El Hameur, M.A., Cerdoun, M., Tarabet, L., Ferrara, G. (2022). CFD flow field assessment and performance map generation of a turbocharger radial turbine attempted to be matched with a downsized diesel engine. In Proceedings of the ASME Turbo Expo 2022: Turbomachinery Technical Conference and Exposition. Rotterdam, Netherlands, p. V007T18A015. https://doi.org/10.1115/GT2022-82212
[30] Liu, Y.M., Spence, S., Horsley, J., Mann, S., Stuart, C. (2024). Insights into turbocharger centrifugal compressor stability using high-fidelity CFD and a novel impeller diffusion factor. In Proceedings of the ASME Turbo Expo 2024: Turbomachinery Technical Conference and Exposition. Volume 12D: Turbomachinery — Multidisciplinary Design Approaches, Optimization, and Uncertainty Quantification; Radial Turbomachinery Aerodynamics; Unsteady Flows in Turbomachinery, London, United Kingdom, p. V12DT35A005. https://doi.org/10.1115/GT2024-123825
[31] Sabahi, A., Tabatabaei, H., Mollayi Barzi, Y. (2024). Improving the performance of the turbocharger turbine by changing its blade inlet angle experimentally and numerically. International Journal of Engine Research, 26(1): 18-26. https://doi.org/10.1177/14680874241265978
[32] Heidary, A.R., Nejat, A., Alaviyoun, S. (2023). CFD study of the impacts of a turbocharger's various wastegate and bypass configurations on the efficiency and the flow field of its radial turbine. Journal of Applied Fluid Mechanics, 16(6): 1145-1159. https://doi.org/10.47176/jafm.16.06.1519

NOMENCLATURE

C_p	specific heat, $J \cdot kg^{-1} \cdot K^{-1}$
G_k	buoyancy production of turbulent kinetic energy, $kg \cdot m^{-1} \cdot s^{-3}$
g	gravitational acceleration, $m \cdot s^{-2}$
k	turbulent kinetic energy, $m^2 \cdot s^{-2}$
K	thermal conductivity, $W \cdot m^{-1} \cdot K^{-1}$
P	static pressure, Pa
P_k	production of turbulent kinetic energy, $kg \cdot m^{-1} \cdot s^{-3}$
T	temperature, K
u, v, w	velocity components in x, y, and z directions, $m \cdot s^{-1}$
$\vec{V}$	velocity vector, $m \cdot s^{-1}$

Greek symbols

ρ	density, $kg \cdot m^{-3}$
μ	dynamic viscosity, $kg \cdot m^{-1} \cdot s^{-1}$
μ_t	turbulent (eddy) viscosity, $kg \cdot m^{-1} \cdot s^{-1}$
ε	rate of dissipation of turbulent kinetic energy, $m^2 \cdot s^{-3}$

β	thermal expansion coefficient, K^{-1}
σ_k	turbulent Prandtl number for k
σ_ε	turbulent Prandtl number for ε
σ_t	turbulent Prandtl number for temperature

Subscripts

t	turbulent quantity
k	kinetic energy related term
ε	dissipation rate related term
x, y, z	spatial coordinates